

# Tensor Network Path Integrals: Implementation and Analysis

Amartya Bose\*

*Department of Chemistry, Princeton University, Princeton, New Jersey 08544*

Peter L. Walters\*

*Department of Chemistry, University of California Berkeley, Berkeley, California 94720 and  
Miller Institute for Basic Research in Science, University of California Berkeley, Berkeley, California 94720*

Tensors with finite correlation afford very compact tensor network representations. A novel tensor network-based decomposition of real-time path integral simulations involving Feynman-Vernon influence functional is introduced. In this tensor network path integral (TNPI) technique, the finite temporarily non-local interactions introduced by the influence functional can be captured very efficiently using matrix product state representation for the path amplitude (PA) tensor. We illustrate this particular TNPI method through various realistic examples, including a charge transfer reaction and an exciton transfer in a dimer. We also show how it is readily applied to systems with greater than two states by simulating a 7-site model of FMO and a molecular wire model. The augmented propagator (AP) TNPI utilizes the symmetries of the problem, leading to accelerated convergence and dramatic reductions of computational effort. We also introduce an approximate method that speeds up propagation beyond the non-local memory length. Furthermore, the structure imposed by the tensor network representation of the PA tensor naturally suggests other factorizations that make simulations for extended systems more efficient. These factorizations would be the subject of future explorations. The flexibility of the AP-TNPI framework makes it a promising new addition to the family of path integral methods for non-equilibrium quantum dynamics.

## I. INTRODUCTION

Quantum mechanics plays an important role in various condensed phase dynamical processes. While there are certain processes, such as calculation of vibrational spectra, that can be simulated using classical mechanics [1], dynamical problems that involve deep tunneling through potential barriers like charge or excitonic transfer are essentially quantum mechanical in nature. Simulation of these quantum processes in condensed phase environments is an extremely challenging task owing to the exponential growth of computational complexity with the degrees of freedom of the system being studied. Wave function-based methods like multi-configuration time-dependent Hartree (MCTDH) [2], its multi-layer version (ML-MCTDH) [3], and time-dependent density matrix renormalization group (tDMRG) [4–6], for example, are extremely powerful in efficiently simulating the dynamics of certain classes of large quantum systems. Tremendous progress has been made in using these wave function-based methods for simulating systems coupled to many degrees of freedom [7–10]. However, if low frequency rovibrational and translational degrees of freedom are involved in the dynamics, the number of extra degrees of freedom that need to be considered explicitly increases, increasing the computational requirements especially at high temperatures. Typically, in the most general case, wave function-based methods are also unable to rigorously describe the thermal equilibrium of systems. These reasons can often render them ill-suited for studying the

dynamics of thermal condensed phase chemical systems when a solvent is involved [11].

Over the years, there has been an explosion of methods that attempt to solve the problem of thermal quantum dynamics in a condensed phase. Most of these methods can be categorized into two groups: approximate methods or quantum-classical methods. Approximate methods tend to treat the entire system under study using “augmented” classical trajectories. The most prominent methods of this group are the various approaches based on the semiclassical approximation [12–16], centroid molecular dynamics [17, 18] and ring polymer molecular dynamics [19–21] for Born-Oppenheimer dynamics, and the family of surface hopping methods [22–25] for non-adiabatic processes. The quantum-classical methods, on the other hand, typically identify a reduced-dimensional quantum “system” and relegate the rest of the degrees of freedom to a classical treatment, thereby effectively restricting the exponential growth of complexity of quantum dynamics to only the system degrees of freedom. Various rigorous quantum-classical approaches have been developed over the years such as quantum-classical Liouville dynamics [26] and quantum-classical path integral (QCPI) [27–30]. Because the system is now treated using exact quantum mechanics all effects stemming from non-adiabaticity are rigorously accounted for.

Amongst the class of problems that can be solved using the system-solvent decomposition, if the solvent can be modelled as a bath of harmonic oscillators, the reduced density matrix of the system can be rigorously simulated without classical trajectories using hierarchical equations of motion (HEOM) [31] and the Feynman-Vernon influence functional (IF) [32]. Though general condensed phase solvents are anharmonic, over

---

\* Both authors contributed equally to this work.

the years, the harmonic bath mapping, obtained via linear response theory, has repeatedly been shown to give impressively accurate results for a variety of systems [33]. While HEOM is, in principle, a completely general method for simulating these systems, in practice, significant challenges arise while simulating the dynamics of a system coupled to a bath that is not described by a Drude spectral density. Recent work has attempted at increasing the applicability of HEOM to more general cases [11, 34–37]. The quasi-adiabatic propagator path integral (QuAPI) [38, 39] and methods based on QuAPI [40–43] enable efficient simulations of the dynamics of systems coupled bi-linearly to harmonic baths. Methods related to QuAPI and HEOM simulate the reduced density matrix. So, the cost does not scale with the number of bath degrees of freedom, and they are able to describe thermal equilibrium accurately. These methods typically model the dynamics of open systems in cases where the system and the solvent have different natures, e.g. a spin system coupled to a reservoir of harmonic bath, and can easily be distinguished. Recently, Lerose *et al.* [44] have developed an influence functional approach for simulating cases where the system and the bath do not have different natures, like identifying one particular spin in a chain of spins as the system.

The biggest challenge in evaluating the real-time path integral is the non-local nature of the IF. This non-Markovian memory leads to an exponential growth of the number of paths that need to be tracked. However, it has a finite length, which means that the entanglement between time points along a path decays after a certain temporal distance. Tensors with finite entanglement can, on many occasions, be very compactly represented using tensor networks. For instance, with extended quantum systems, the dimensionality of the Hilbert space grows exponentially with the number of particles. However, matrix-product states (MPSs) and other tensor network decompositions allow efficient representations of many such systems. This is why TN structures are used to efficiently represent the wave function in DMRG [5, 45–49] and other methods optimized for simulating multiple dimensions and critical phenomena like the projected entangled-pair state (PEPS) [50] and the multiscale entanglement renormalization ansatz (MERA) [51, 52]. Of late, using tensor network algorithms for simulating open quantum systems has also been gaining popularity [44, 53–56]. In this paper, we introduce and critically evaluate a similar tensor-network method for performing path integral simulations for systems coupled with a dissipative medium using the QuAPI splitting [57, 58]. This method, the augmented propagator-based tensor network path integral (AP-TNPI), uses MPSs to compress the representation of the path amplitude (PA) tensor involved in path integral simulations. Consequently, the influence functional becomes a matrix-product operator (MPO) that acts on the PA MPS. As opposed to the other numerical approaches for defining these matrix product structures [53, 55, 59], by a clean separation

of the path amplitude tensor from the influence functional MPO and through a careful analytical construction of the latter, we exploit inherent symmetries present in the problem giving closed form expressions to it. In this work, we utilize the open source ITensor library [60] as the basis of our AP-TNPI implementation, as it provides for an efficient means of evaluating the relevant tensor operations.

In Sec. II, we discuss the AP-TNPI method, detailing a construction that results in a simple, elegant and efficient structure. We also demonstrate an approximation that emerges naturally from the resulting structure. This “Markovian iteration scheme” approximation is able to speed up simulations involving processes with very long time-scales and comparatively short memory lengths. Thereafter, in Sec. III, we illustrate the use of the method through numerous examples. Apart from a direct comparison with QuAPI and related methods, we apply AP-TNPI to study charge and exciton transfer dynamics. We demonstrate the ability of AP-TNPI to develop an optimized representation enabling us to access long memory times even with very modest computational resources. Finally, we end the paper in Sec. IV with some concluding remarks, and outlook for further developments based on, and facilitated by AP-TNPI.

## II. METHODOLOGY

Consider a potentially time-dependent quantum system interacting bi-linearly with a harmonic bath. The Hamiltonian is given as:

$$\hat{H} = \hat{H}_0(t) + \hat{H}_b(\hat{\mathbf{x}}, \hat{\mathbf{p}}, \hat{s}) \quad (1)$$

$$\hat{H}_b(\hat{\mathbf{x}}, \hat{\mathbf{p}}, \hat{s}) = \sum_j \frac{\hat{p}_j^2}{2m_j} + \frac{1}{2}m_j\omega_j^2 \left( \hat{x}_j - \frac{c_j\hat{s}}{m_j\omega_j^2} \right)^2 \quad (2)$$

where  $\hat{H}_0(t)$  is the Hamiltonian of the isolated  $D$ -state quantum system, and  $\hat{H}_b$  is the Hamiltonian for the bath and the system-bath interactions. These interactions are defined in terms of  $\omega_j$  and  $c_j$ , which are the frequency and the coupling strength of the  $j^{\text{th}}$  bath mode, respectively. The system position operator is  $\hat{s}$ . The system-bath interaction is characterized by the spectral density [61]:

$$J(\omega) = \frac{\pi}{2} \sum_j \frac{c_j^2}{m_j\omega_j} \delta(\omega - \omega_j). \quad (3)$$

The spectral density is related to the energy gap autocorrelation function via a Fourier transform [33]. For most classical solvents, this autocorrelation function is computed using classical trajectories on an appropriately parameterized force field.

The dynamics of the isolated  $D$ -state system can be obtained by directly solving the time-dependent Schrödinger equation for the propagator:

$$i\hbar \frac{\partial \hat{U}_0(t_0, t)}{\partial t} = \hat{H}_0(t) \hat{U}_0(t_0, t), \quad (4)$$

where  $\hat{U}_0(t_0, t)$  is the propagator evolving the system from an initial state at time  $t_0$  to a final state at time  $t$ . The density matrix is propagated using a combination of forward and backward propagators; this combined forward-backward propagator,  $K_j$ , connecting states at time point  $t_0 = (j-1)\Delta t$  to  $t = j\Delta t$  is given by:

$$K_j (s_{j-1}^\pm, s_j^\pm, \Delta t) = \langle s_j^+ | \hat{U}_0((j-1)\Delta t, j\Delta t) | s_{j-1}^+ \rangle \\ \times \langle s_{j-1}^- | \hat{U}_0^\dagger((j-1)\Delta t, j\Delta t) | s_j^- \rangle \quad (5)$$

where  $s_j^\pm$  is the forward-backward state of the system at the  $j^{\text{th}}$  time point discretized according to QuAPI splitting [57, 58].

Suppose that the system and bath are initially uncoupled and that the bath is in a thermal equilibrium  $\rho_b(\beta)$  at an inverse temperature of  $\beta$ . The reduced density matrix at a final time,  $\langle s_N^+ | \tilde{\rho}(N\Delta t) | s_N^- \rangle = \tilde{\rho}(s_N^\pm, N\Delta t)$ , can be obtained using a discretized path integral representation as follows:

$$\tilde{\rho}(s_N^\pm, N\Delta t) = \text{Tr}_b \langle s_N^+ | \hat{U}(t) \tilde{\rho}(0) \otimes \rho_b(\beta) \hat{U}^\dagger(t) | s_N^- \rangle \\ = \sum_{s_0^\pm} \tilde{\rho}(s_0^\pm, 0) G(s_0^\pm, s_N^\pm, N\Delta t) \quad (6)$$

$$G(s_0^\pm, s_N^\pm, N\Delta t) = \sum_{s_1^\pm} \cdots \sum_{s_{N-1}^\pm} K_1(s_0^\pm, s_1^\pm, \Delta t) \\ \times K_2(s_1^\pm, s_2^\pm, \Delta t) \\ \cdots K_N(s_{N-1}^\pm, s_N^\pm, \Delta t) F[\{s_j^\pm\}] \quad (7)$$

where  $\Delta t$  is the quantum time-step that was used to discretize the path integral. The augmented propagator for the reduced system, or the Green's function, connecting state  $s_0$  to  $s_k$  in  $k$  time steps is  $G(s_0^\pm, s_k^\pm, k\Delta t)$  and  $\hat{U}$  is the full system-bath propagator. The Feynman-Vernon influence functional [32],  $F[\{s_j^\pm\}]$ , encodes the interaction of the system with the bath and is given as

$$F[\{s_j^\pm\}] = \exp \left( -\frac{1}{\hbar} \sum_{0 \leq k \leq N} \Delta s_k \sum_{0 \leq k' \leq k} (\text{Re}(\eta_{kk'}) \Delta s_{k'} \\ + 2i \text{Im}(\eta_{kk'}) \bar{s}_{k'}) \right) \quad (8)$$

where  $\eta_{kk'}$  are the discretized  $\eta$ -coefficients [38, 39],  $\Delta s_k = s_k^+ - s_k^-$  and  $\bar{s}_k = \frac{1}{2}(s_k^+ + s_k^-)$ .

First, we define a couple terms that we use to rephrase the problem and build the TNPI algorithm. Consider the bare and full variants of the path amplitude tensor defined respectively as:

$$P_{s_0^\pm \dots s_N^\pm}^{(0)} = K_1(s_0^\pm, s_1^\pm, \Delta t) K_2(s_1^\pm, s_2^\pm, \Delta t) \\ \cdots K_N(s_{N-1}^\pm, s_N^\pm, \Delta t) \quad (9)$$

$$P_{s_0^\pm \dots s_N^\pm} = F[\{s_j^\pm\}] P_{s_0^\pm \dots s_N^\pm}^{(0)} \quad (10)$$

The quantities  $P^{(0)}$  and  $P$  are tensors of rank  $N$  with  $O(D^{2N})$  coefficients. The bare PA tensor,  $P^{(0)}$ , contains the full information about the bare system propagation. Information regarding any time-dependence of the system Hamiltonian,  $H_0$  is also included here. The augmented propagator is obtained from the full PA tensor by contracting over all but the terminal indices.

$$G(s_0^\pm, s_N^\pm, N\Delta t) = \sum_{s_1^\pm} \cdots \sum_{s_{N-1}^\pm} P_{s_0^\pm \dots s_N^\pm} \quad (11)$$

Since the number of values required to describe the PA tensor grows exponentially with the number of time steps, a direct evaluation of the augmented propagator is only possible if the number of time steps is small. The goal of using tensor networks is to “factorize” these large tensors into products of many smaller ones; and thus, reduce the cost of evaluation and storage. The optimum structure of the tensor network involved is guided strongly by the exact nature of the tensor under consideration.

It is well known that the non-Markovian memory length of a quantum system interacting with a condensed phase is not infinitely long. Though these non-local interactions do not have a finite support, they decay asymptotically. The relative short-ranged nature of the interaction between time-points imply that the PA tensor should be well described as a sequence of tensor products, where each tensor corresponds to a different time-point. The resulting factorization gives

$$P_{s_0^\pm \dots s_N^\pm} = \sum_{\{\alpha_j\}} M_{\alpha_0}^{s_0^\pm} M_{\alpha_0, \alpha_1}^{s_1^\pm} \cdots M_{\alpha_{N-2}, \alpha_{N-1}}^{s_{N-1}^\pm} M_{\alpha_{N-1}}^{s_N^\pm} \quad (12)$$

which is the MPS representation of the PA tensor. In this representation, each tensor in the product is considered to be on a different site. The indices that are used in the superscript are the so-called “site indices” and they correspond to the forward-backward state of the system at the different time points. The indices in the subscript,  $\{\alpha_j\}$ , are the so-called “bond indices,” the dimensions of which are closely related to the length of the non-Markovian memory. Two relevant quantities that govern the understanding of methods based on matrix product structures are the maximum bond dimension,  $m = \max(\dim(\alpha_j))$ , and the average or typical bond dimension,  $\frac{1}{N} \sum_j \dim(\alpha_j)$ . In principle this factorization is exact; however, for an arbitrary PA tensor, the maximum bond dimension is  $O(D^N)$ . In practice, the bond dimensions are truncated and treated as convergence parameters. As we can see from Eq. (12), truncating the bonds do not change the number of paths; therefore, all paths are always considered. We will show in Sec. III, that the actual bond dimensions needed in a simulation are quite small.

The presence of the influence functional in the description of the full PA tensor (Eq. (10)) prevents us from forming simple expressions for the tensors in Eq. (12);

however, as we will now show, this is not the case for the bare PA tensor. Consider the singular value decomposition (SVD) of the forward-backward propagator:

$$K_j (s_{j-1}^\pm, s_j^\pm, \Delta t) = \sum_{\alpha_{j-1}} U_{\alpha_{j-1}}^{s_{j-1}^\pm} \times R_{\alpha_{j-1}}^{s_j^\pm} \quad (13)$$

$$R_{\alpha_{j-1}}^{s_j^\pm} = \sum_{\beta} S_{\alpha_{j-1}, \beta} \times V_{\beta}^{s_j^\pm \dagger} \quad (14)$$

where  $S$  is the diagonal matrix of the nonzero singular values,  $U$  and  $V$  are the matrices of the left and right singular vectors respectively. Substituting this into Eq. (9), we get the required expressions for the tensors appearing in Eq. (12). Thus, for a bare PA MPS:

$$M_{\alpha_0}^{s_0^\pm} = U_{\alpha_0}^{s_0^\pm}, \quad (15)$$

$$M_{\alpha_{N-1}}^{s_{N-1}^\pm} = R_{\alpha_{N-1}}^{s_{N-1}^\pm}, \quad (16)$$

$$M_{\alpha_{j-1}, \alpha_j}^{s_{j-1}^\pm, s_j^\pm} = R_{\alpha_{j-1}}^{s_{j-1}^\pm} U_{\alpha_j}^{s_j^\pm} \quad 0 < j < N. \quad (17)$$

It is worth noting that, in this case, the factorization is exact, and the bond dimensions are independent of the number of time-steps,  $N$ . This is a direct consequence of the Markovian nature of the system dynamics. We schematically depict the bare PA as an MPS with red circular nodes as in Fig. 1.

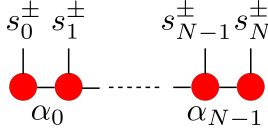


FIG. 1. Schematic diagram for bare PA MPS. Red nodes denote the matrices corresponding to the bare system propagator's SVD.

Now that we have described how to deal with the bare system, let us consider the influence functional. From Eq. (10), we see that to obtain the full PA MPS, the influence functional must be applied to the bare PA MPS. In the TN framework, a MPO acts on a MPS to produce another MPS; therefore, we want to construct an influence functional MPO, which, when applied to the bare PA MPS, gives the PA MPS for the full system-bath problem. The full influence functional can be rewritten as a product of terms coming from the interactions with different end-points

$$F [\{s_j^\pm\}] = \prod_{0 \leq k \leq N} F_k [\{s_j^\pm\}] \quad (18)$$

$$F_k [\{s_j^\pm\}] = \exp \left( -\frac{1}{\hbar} \Delta s_k \sum_{0 \leq k' \leq k} (\text{Re}(\eta_{kk'}) \Delta s_{k'} + 2i \text{Im}(\eta_{kk'}) \bar{s}_{k'}) \right). \quad (19)$$

The influence functional corresponding to a particular end time point,  $F_k [\{s_j^\pm\}]$  given by Eq. (19), can be expressed as an MPO. We will construct this MPO in two steps by grouping the forward-backward states by the unique values of  $\Delta s$ . First, consider the trivial case when  $\Delta s_k = 0$ , and note that for all these states,  $F_k = 1$ , or as an operator,  $F_k = \mathbb{I}^{s_0^\pm} \otimes \mathbb{I}^{s_1^\pm} \dots \mathbb{I}^{s_{k-1}^\pm} \otimes \mathcal{P}_0^{s_k^\pm}$  where  $\mathbb{I}^{s_j^\pm}$  is the identity operator in the space of  $\{s_j^\pm\}$ , and  $\mathcal{P}_0^{s_k^\pm}$  is the projection operator on to the space where  $\Delta s_k = 0$ .

Next, we consider a non-zero value of  $\Delta s_k$ . For all these states, the operators on sites,  $k' < k$ , are given as  $e^{-\frac{1}{\hbar} \Delta s_k (\text{Re}(\eta_{kk'}) \mathbb{D}_{k'} + 2i \text{Im}(\eta_{kk'}) \mathbb{S}_{k'})}$ , and the operator on site  $k' = k$  as  $\mathcal{P}_{\Delta s_k}^{s_k^\pm} e^{-\frac{1}{\hbar} \Delta s_k (\text{Re}(\eta_{kk}) \mathbb{D}_k + 2i \text{Im}(\eta_{kk}) \mathbb{S}_k)}$ . Here  $\mathbb{D}_k$  and  $\mathbb{S}_k$  are the matrices that return the difference and average position of the system corresponding to the forward-backward state. Both the  $\mathbb{D}$  and  $\mathbb{S}$  operators are diagonal in the  $s^\pm$  basis. For this particular value of  $\Delta s_k$ , the resulting  $F_k$ , becomes direct product of these single site operators. Therefore,  $F_k$  can be represented as a sum of direct product of operators, where each term in the sum corresponds to a different value of  $\Delta s_k$ . Hence, we can define  $F_k$  as a MPO,  $\mathbb{F}_k$ , as follows:

$$\mathbb{F}_k = \sum_{\{\beta_j\}} W_{\beta_0}^{s_0^\pm, s_0'^\pm}(\eta_{k0}) \dots W_{\beta_{k'-1}, \beta_{k'}}^{s_{k'}^\pm, s_{k'}'^\pm}(\eta_{kk'}) \times W_{\beta_{k'}, \beta_{k'+1}}^{s_{k'+1}^\pm, s_{k'+1}'^\pm}(\eta_{k(k'+1)}) \dots W_{\beta_{k-1}}^{s_k^\pm, s_k'^\pm}(\eta_{kk}) \quad (20)$$

where  $\{\beta_j\}$  are the bond indices. In this case, all the bond dimensions of this MPO are equal to the number of unique values of  $\Delta s$ . We define  $f(\beta)$  as the function that when given a value of the bond index  $\beta$ , returns the corresponding value of  $\Delta s$ . Furthermore, we define  $\mathcal{P}_{f(\beta)}^{s_k^\pm}$  to be the projection operator on to the space where  $\Delta s_k = f(\beta)$ . With this notation, now, we can define the various tensors in our influence functional MPO.

$$W_{\beta_0}^{s_0^\pm, s_0'^\pm}(\eta_{k0}) = \delta_{s_0^\pm, s_0'^\pm} \exp \left( -\frac{1}{\hbar} f(\beta_0) (\text{Re}(\eta_{k0}) \Delta s_0 + 2i \text{Im}(\eta_{k0}) \bar{s}_0) \right) \quad (21)$$

$$W_{\beta_{k'-1}, \beta_{k'}}^{s_{k'}^\pm, s_{k'}'^\pm}(\eta_{kk'}) = \delta_{s_{k'}^\pm, s_{k'}'^\pm} \delta_{\beta_{k'-1}, \beta_{k'}} \exp \left( -\frac{1}{\hbar} f(\beta_{k'-1}) (\text{Re}(\eta_{kk'}) \Delta s_{k'} + 2i \text{Im}(\eta_{kk'}) \bar{s}_{k'}) \right) \quad (22)$$

$$W_{\beta_{k-1}}^{s_k^\pm, s_k'^\pm}(\eta_{kk}) = \delta_{s_k^\pm, s_k'^\pm} \mathcal{P}_{f(\beta_{k-1})}^{s_k^\pm} \exp\left(-\frac{1}{\hbar} \Delta s_k (\text{Re}(\eta_{kk}) \Delta s_k + 2i \text{Im}(\eta_{kk}) \bar{s}_k)\right) \quad (23)$$

Because  $\mathbb{F}_k$  is an MPO representation of the influence functional terms, it is invariant to any external time-dependence that the system Hamiltonian might have. This analytic form of the IF MPO encodes the invariance of the influence functional with respect to the average forward-backward system states,  $\bar{s}_k$ , present in the form of Eq. (8). This symmetry is also used by the blip-summed path integral [40, 41] (BSPI) method as its starting point. General algorithms have recently been developed to numerically generate the full IF MPO,  $\mathbb{F} = \prod_k \mathbb{F}_k$ , for a larger class of solvents [55, 59] instead of the  $\{\mathbb{F}_k\}$  used here. While it might, in principle, be possible to compress  $\mathbb{F}_k$  [62, 63], we do not foresee a great computational benefit. The analytical expressions already utilize the inherent structure to construct an optimally compressed representation. Additionally, it has been shown that filtration strategies involving QuAPI influence functional generally work best when applied to the product of the bare propagator and the IF [40, 41, 64, 65].

The MPS representation of the full PA tensor can be obtained by iteratively applying the  $\mathbb{F}_k$  MPOs to the bare PA MPS.

$$P_{s_0^\pm, s_1^\pm}^{(1)} = \sum_{\{\alpha'_j\}} \mathbb{F}_1 P_{s_0'^\pm, s_1'^\pm}^{(0)} \quad (24)$$

$$P_{s_0^\pm \dots s_k^\pm}^{(k)} = \sum_{\{\alpha'_j\}} \mathbb{F}_k \left( P_{s_0'^\pm \dots s_{k-1}'^\pm}^{(k-1)} K_{\alpha_{k-1}}^{s_{k-1}^\pm, s_k^\pm} \right) \quad (25)$$

$$P_{s_0^\pm \dots s_N^\pm} = \sum_{\{\alpha'_j\}} \mathbb{F}_N \left( P_{s_0'^\pm \dots s_{N-1}'^\pm}^{(N-1)} K_{\alpha_{N-1}}^{s_{N-1}^\pm, s_N^\pm} \right) \quad (26)$$

where  $\{\alpha'_j\}$  are the new bonds indices produced by the application of the MPO to the MPS. In the above expressions,  $P_{s_0^\pm \dots s_k^\pm}^{(k)}$  represents the PA MPS after the  $k^{\text{th}}$  step of the propagation, and the tensor  $K_{\alpha_{k-1}}^{s_{k-1}^\pm, s_k^\pm} = U_{\alpha_{k-1}}^{s_{k-1}^\pm} R_{\alpha_{k-1}}^{s_k^\pm}$  and is associated with the SVD decomposition of the  $k^{\text{th}}$  forward-backward system propagator,  $K_k(s_{k-1}^\pm, s_k^\pm, \Delta t)$  (see Eqs. (5), (9), (13) and (14)). The first couple of steps of the application of the IF MPO are schematically portrayed in Fig. 2. We would like to note that this clean separation of the bare path amplitude being the MPS and the influence functional being the MPO is not achieved in the time-evolving matrix product operator method (TEMPO) [53].

As we discussed earlier, the non-Markovian memory in a condensed phase process decays to zero, thus we can construct an accurate MPS representation of the PA tensor using fairly small values for the bond dimensions. However, the bond dimensions can be further reduced by explicitly truncating the memory. To that end, we

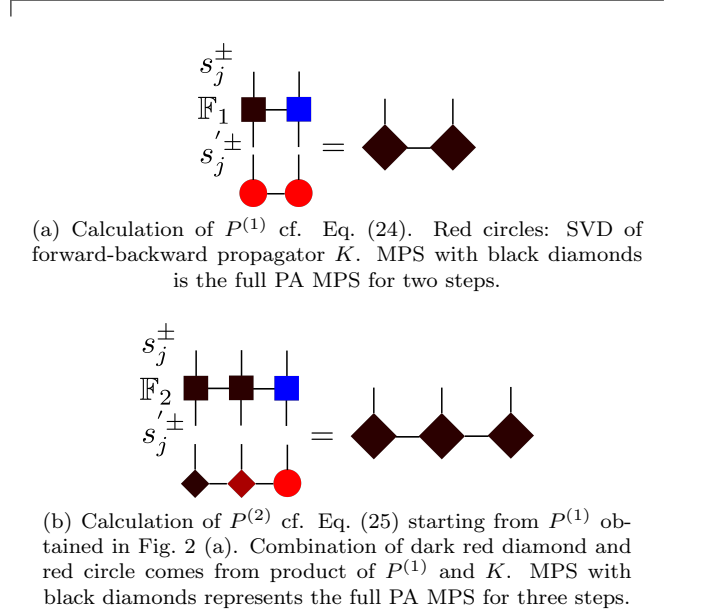


FIG. 2. Schematic diagrams for application of IF MPO.

define  $L\Delta t$  to be the maximum distance, in time, between which the influence functional can couple two forward-backward system points. We see from Eq. (7) that any system points that exceed this difference can be summed independently of each other. This leads us to define the partially contracted PA MPS, as well as the partially contracted IF MPO:

$$\tilde{P}_{s_0^\pm, s_{N-L}^\pm \dots s_N^\pm} = \sum_{s_1^\pm} \dots \sum_{s_{N-L-1}^\pm} P_{s_0^\pm \dots s_N^\pm}, \quad L < N \quad (27)$$

$$\begin{aligned} \tilde{\mathbb{F}}_k &= \sum_{\{\beta_j\}} W_{\beta_0}^{s_0^\pm, s_0'^\pm} (0) W_{\beta_0, \beta_{k-L}}^{s_{k-L}^\pm, s_{k-L}'^\pm} (\eta_{k(k-L)}) \\ &\dots W_{\beta_{k-1}, \beta_{k'}}^{s_{k-1}^\pm, s_{k'}^\pm} (\eta_{kk'}) \dots W_{\beta_{k-1}}^{s_k^\pm, s_k'^\pm} (\eta_{kk}), \quad L < k \quad (28) \end{aligned}$$

where the  $W$  tensors are the same as those defined earlier (see Eqs. (21), (22) and (23)).

We can now redefine the iterative procedure described above for calculating the full PA MPS, in a manner consistent with an explicit truncation of the memory. When  $k \leq L$ , the procedure follows Eqs. (24) and (25) exactly. This is called the “full memory” regime. When  $k > L$ , which is often referred to as the “iteration” regime, we have

$$\tilde{P}_{s_0^\pm \dots s_{L+1}^\pm}^{(L+1)} = \sum_{\{\alpha'_j\}} \tilde{\mathbb{F}}_{L+1} P_{s_0'^\pm \dots s_L'^\pm}^{(L)} K_{\alpha_L}^{s_L^\pm, s_{L+1}^\pm} \quad (29)$$

$$\tilde{P}_{s_0^\pm, s_{k-L}^\pm \dots s_k^\pm}^{(k)} = \sum_{\{\alpha'_j\}} \tilde{\mathbb{F}}_k \left( \sum_{s_{k-L-1}^\pm} \tilde{P}_{s_0'^\pm, s_{k-L-1}'^\pm \dots s_{k-1}'^\pm}^{(k-1)} \right)$$

$$\times K_{\alpha_{k-1}}^{s_{k-1}^{\pm}, s_k^{\pm}} \Big) \quad (30)$$

$$\begin{aligned} \tilde{P}_{s_0^{\pm}, s_{N-L}^{\pm} \dots s_N^{\pm}}^{(N)} = & \sum_{\{\alpha_j'\}} \tilde{\mathbb{F}}_N \left( \sum_{s_{N-L-1}^{\pm}} \tilde{P}_{s_0^{\pm}, s_{N-L-1}^{\pm} \dots s_{N-1}^{\pm}}^{(N-1)} \right. \\ & \left. \times K_{\alpha_{N-1}}^{s_{N-1}^{\pm}, s_N^{\pm}} \right) \quad (31) \end{aligned}$$

Due to the aforementioned memory truncation, the number of system sites never exceeds  $L + 2$ . Lastly, the expression for the augmented propagator in terms of the partially contracted PA MPS is given by

$$G(s_0^{\pm}, s_N^{\pm}, N\Delta t) = \sum_{s_{N-L}^{\pm}} \dots \sum_{s_{N-1}^{\pm}} \tilde{P}_{s_0^{\pm}, s_{N-L}^{\pm} \dots s_N^{\pm}}. \quad (32)$$

As it turns out, this iterative procedure is very similar to the one used by iterative QuAPI. The key difference is that iterative QuAPI [38, 39] and related methods [40, 41], including ones based on tensor networks [54, 55] such as TEMPO [53], sums over  $s_0^{\pm}$  as soon as  $k > L$ , but here, it is retained as part of the PA MPS and consequently the augmented propagator. It is interesting that this calculation of the augmented propagator requires negligible additional cost in the AP-TNPI framework. Apart from being important for evaluation of the memory kernel associated with the Nakajima-Zwanzig [66, 67] generalized quantum master equation [68–72], calculating the augmented propagator also allows the simulation to be independent of initial state of the system. The small matrix decomposition of path integrals (SMatPI) [42, 43], which is designed to minimize the storage requirements to roughly that of the reduced density matrix, is also defined in terms of this augmented propagator.

There are various algorithms for applying an MPO to an MPS. Probably the two most common methods are the direct application followed by an SVD-based compression of the MPS and a variational application of the MPO to the MPS. Paeckel *et al.* [73] have provided a detailed overview of these methods, the computational effort involved and the common pitfalls. The scaling of the variational MPO-MPS application for an MPS of length  $l$  goes as  $O(dlm^3w)$ , if the maximum MPS bond dimension is  $m$ , the MPO bond dimension is  $w$ , and the site dimension is  $d$  [73]. The site dimension is related to the dimensionality of the quantum system as  $d = D^2$ . Though it is well-known that the variational method can, depending on the initial “guess” MPS, get stuck in metastable states, in our current explorations we have faced no such issues. This might be because for a given time-step, the individual  $\mathbb{F}_k$  and  $\tilde{\mathbb{F}}_k$  do not significantly alter the MPSs. It is interesting to note that this “perturbative” impact of the influence functional MPO on the path amplitude

MPS is a result of the particular decomposition achieved by separating the bare propagator part completely from the influence functional. However, we still checked all the calculations reported against the direct SVD method as well.

In addition to the iterative algorithms we have outlined till now, AP-TNPI allows a different approach that uses the augmented propagator between  $t = 0$  and  $t = L\Delta t$  to approximate the propagation when the Hamiltonian is time-independent:

$$\tilde{\rho}(s_k^{\pm}, k\Delta t) = \sum_{s_0^{\pm}} G(s_0^{\pm}, s_k^{\pm}, k\Delta t) \tilde{\rho}(s_0^{\pm}, 0), \quad \text{when } k \leq L \quad (33)$$

$$\begin{aligned} \tilde{\rho}(s_k^{\pm}, k\Delta t) \approx & \sum_{s_{k-L}^{\pm}} G(s_0^{\pm}, s_L^{\pm}, L\Delta t) \\ & \times \tilde{\rho}(s_{k-L}^{\pm}, (k-L)\Delta t) \delta_{s_{k-L}^{\pm}, s_0^{\pm}}, \quad \text{otherwise.} \quad (34) \end{aligned}$$

We call this scheme the Markovian iteration TNPI scheme (MTNPI). While it is exact within memory, MTNPI misses out on some interactions present in the canonical iteration scheme, and consequently converges slower with respect to  $L$ . However, if this increased memory can be spanned, the iteration is just a sequence of matrix-vector multiplications, and hence very fast. Even when memory is not converged, this method results in computationally cheap dynamics that is quite physically insightful. This computational advantage becomes especially important when the total time-scale of the dynamics far exceeds the length of the non-Markovian memory.

Please note that while for simplicity the entire development in this section has been done in terms of a bilinearly coupled bath that interacts with the “position” operator of the system, this is not a necessary restriction. The formalism of Feynman-Vernon influence functional is general, and consequently AP-TNPI can also be extended to deal with other couplings. The more general expressions presented in Refs. [74, 75] are summarized in Appendix A for convenience.

### III. RESULTS

We will now apply AP-TNPI to a large variety of illustrative examples. This section is organized as follows: first, we benchmark the method on two-level systems against other path integral methods. We try to understand the behavior of the bond dimensions and convergence in general. We show that AP-TNPI can easily simulate dynamics which can only be treated with more recent techniques [30, 40–43]. Then, we apply AP-TNPI to two realistic applications: a charge transfer example and excitonic dynamics in a dimer. For the charge transfer, using a combination of rate theory and direct dynamics, we try to understand the essential physics, whereas for the excitonic dynamics, we are able to converge the

relevant dynamics directly. Finally, we show examples of applying AP-TNPI to multilevel systems.

Before continuing to the results, a brief mention of the convergence parameters is in order. Apart from the standard time step ( $\Delta t$ ) and memory length ( $L$ ) associated with iterative path integral methods, AP-TNPI has two additional controllable parameters: the maximum allowable bond dimension ( $M$ ), and the truncation threshold ( $\chi$ ). While the precise meaning of the truncation threshold depends of the exact nature of the compression algorithm used, here it can be thought of as a SVD-like truncation, where any singular values smaller than the given threshold are omitted. More specifically, the singular values,  $\lambda_n$ , are discarded such that

$$\frac{\sum_{n \in \text{discarded}} \lambda_n^2}{\sum_n \lambda_n^2} < \chi. \quad (35)$$

These four parameters are interrelated, therefore, the convergence is ultimately a search procedure to find the combination that gives the correct dynamics at the least cost. For simplicity, we generally have not explicitly constrained the maximum bond dimension.

### A. Two-level systems

Two-level systems (TLS) are some of the most commonly studied model systems in quantum dynamics. They are relatively simple and yet support a surprisingly rich array of dynamics. As the name implies, the system is described by a Hamiltonian with 2 states:

$$\hat{H}_0 = \sum_{j=1}^2 \epsilon_j |\sigma_j\rangle\langle\sigma_j| - \hbar\Omega (|\sigma_1\rangle\langle\sigma_2| + |\sigma_2\rangle\langle\sigma_1|), \quad (36)$$

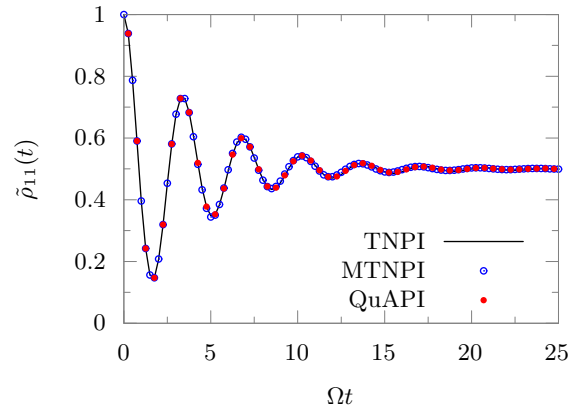
where  $|\sigma_1\rangle$  and  $|\sigma_2\rangle$  are eigenstates of the system's position operator,  $\hat{s}$ , i.e.,  $\hat{s}|\sigma_j\rangle = \sigma_j|\sigma_j\rangle$ ; throughout this subsection, this pair of eigenvalues,  $\{\sigma_1, \sigma_2\}$ , will be referred to as the the system's coordinates. Additionally, the position dependent energies are defined as  $\epsilon_1 = \epsilon$  and  $\epsilon_2 = -\epsilon$ . With this model, the key parameters are the asymmetry,  $\epsilon$ , and the tunneling splitting of  $2\hbar\Omega$ . All the examples in this subsection use Eq. (36) as the Hamiltonian for the isolated system.

#### 1. Benchmark calculations

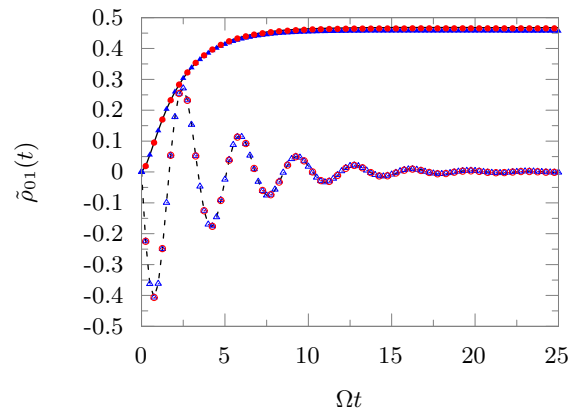
For the benchmark calculations, we track the population decay of the system. More specifically, we simulate  $\langle 1|\tilde{\rho}(t)|1\rangle$ , where  $\langle 1|\tilde{\rho}(0)|1\rangle = 1$ . The system is taken to be coupled bi-linearly with a harmonic bath as described by Eq. (2), with the spectral density having the Ohmic form

$$J(\omega) = \frac{\pi}{2} \hbar \xi \omega \exp\left(-\frac{\omega}{\omega_c}\right). \quad (37)$$

Here,  $\xi$  is the dimensionless Kondo parameter that characterizes the system-bath coupling, and  $\omega_c$  is the cutoff frequency of the bath. To keep these calculations general, the parameters are given in terms of  $\Omega$ .



(a) Population dynamics



(b) Off-diagonal terms. Solid line, markers:  $\text{Re}(\tilde{\rho}_{01})$ . Dashed line, hollow markers:  $\text{Im}(\tilde{\rho}_{01})$ . Lines: TNPI. Red circles: iQuAPI. Blue triangles: MTNPI

FIG. 3. Comparison with QuAPI for typical spin-boson parameters. Bath is characterized by  $\hbar\Omega\beta = 5$ ,  $\omega_c = 7.5\Omega$ ,  $\xi = 0.1$ ,  $\chi = 10^{-6}$ .

In Fig. 3, we compare fully converged AP-TNPI results with QuAPI for a symmetric ( $\epsilon = 0$ ) system interacting weakly with a cold, fast harmonic bath, as represented by  $\hbar\Omega\beta = 5$ ,  $\omega_c = 7.5\Omega$  and  $\xi = 0.1$ . The system's coordinates are  $\{1, -1\}$ . Because there are no additional approximations, both AP-TNPI and QuAPI converge with exactly the same  $\Omega\Delta t = 0.25$  and  $L = 8$ . The same level of compression was used to converge both the diagonal and the off-diagonal terms of the RDM. We show the converged results for MTNPI done at  $L = 15$ . Despite the additional memory introduced by the simplified MTNPI propagation scheme, the basic physics is still reproduced. For this parameter, using MTNPI we were able to reproduce the population curves and the imaginary part of  $\rho_{01}$  exactly. Though rather accurate, there

is a very slight discrepancy in the MTNPI estimation of the real part of  $\rho_{01}$ .

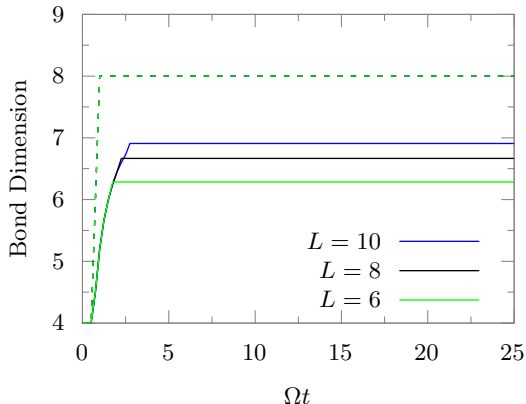


FIG. 4. Growth of average (solid) and maximum (dashed) bond dimensions of PA MPS with time and  $L$  for parameters shown in Fig. 3 calculated with  $\chi = 10^{-6}$ .

Before showing more computationally intensive examples, let us analyze the growth of the bond dimension with the memory length  $L$  and the cutoff  $\chi$  for the simple case of Fig. 3. In Table I, we show the maximum and average bond dimensions corresponding to calculations with particular memory length,  $L$ , at the end of the simulation time of  $\Omega t = 25$ , and the average root-mean-square (RMS) deviation for all the RDM elements from the most accurate simulation done. Since the cost of the MPO-MPS application scales as the cube of the average MPS bond dimension [73], setting  $\chi = 0$  results in a calculation that is even more costly than QuAPI. However, even with a minimal value of  $\chi > 0$ , there is a dramatic reduction of the bond dimensions. Additionally, we see that when the memory length is far from convergence, it is difficult to judge the convergence of  $\chi$ , and vice versa. (While it is interesting to study the RMS errors for these benchmark simulations, it cannot serve as a sole guide to convergence. This is particularly true, if the results aren't known beforehand. When unconverged, the dynamics may still show unphysical behaviors despite the calculated error being quite small.) The time-dependence of the average bond-dimension for different values of  $L$  near convergence is given in Fig. 4. Here, we see that during the iteration, the bond-dimension remains practically constant; therefore, the computational cost scales linearly with the number of steps. Notice that for this problem, the converged cutoff is high enough that the maximum bond dimension for all three memory lengths is the same.

In Fig. 5, we consider a symmetric TLS ( $\epsilon = 0$ ) strongly coupled ( $\xi = 2$ ) to a sluggish bath ( $\omega_c = \Omega$ ) [30, 76]. The system's coordinates are  $\{0, -2\}$ , i.e., the bath is initially equilibrated to the populated state of the system. Here,  $\Omega\Delta t = 0.125$  and  $\chi = 10^{-10}$ . The strong coupling and sluggish bath imply that the non-

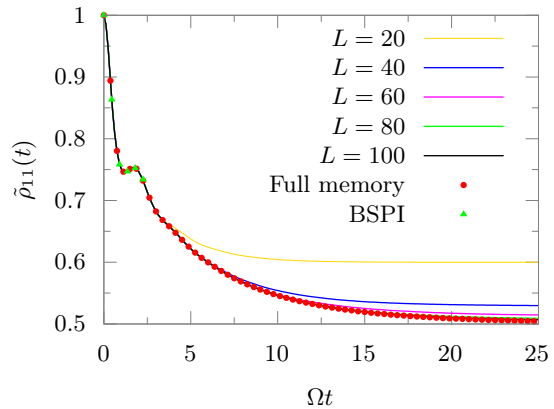


FIG. 5. Simulation with very long non-Markovian memory:  $\epsilon = 0$ ,  $\hbar\Omega\beta = 1$ ,  $\omega_c = \Omega$ ,  $\xi = 2$ . BSPI results are shown up to the point where they could be converged.

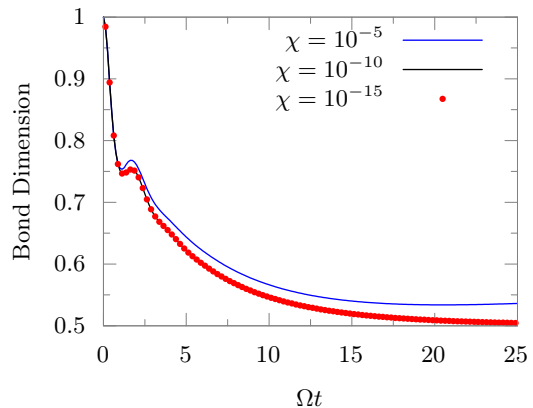


FIG. 6. Dynamics for different values of  $\chi$  when  $M$  is left unconstrained. Parameters same as Fig. 5. These are full memory calculations.

Markovian memory is quite long. Generally, this is the regime where iterative QuAPI performs the worst. It is interesting to note that with AP-TNPI, owing to the compressions enabled by the MPS representation, we can converge the dynamics directly till equilibration of the system around  $\Omega t \approx 25$ , reproducing results previously obtained by SMatPI [77]. Convergence is reached at a memory length of  $L = 100$ . In this particular case, AP-TNPI was remarkably successful at compressing the PA MPS, which at the final time point of  $\Omega t = 25$  has an average bond dimension of  $M = 35.96$ . For comparison, we were unable to converge the full dynamics using blip-summed path integral (BSPI) [40, 41]. This is because though this is a case of a strongly coupled slow bath, the conditions are not close enough to an incoherent decay to enable convergence based on the filtration by the number of blips, i.e. time points where  $\Delta s \neq 0$ .

We also simulate the full memory dynamics using various cutoffs in Fig. 6. Even at a fairly large cutoff of

L	$10^{-4}$	$10^{-6}$	$10^{-8}$	$10^{-10}$	$10^{-12}$	0
2	4, 4, 0.026	4, 4, 0.026	4, 4, 0.026	4, 4, 0.026	4, 4, 0.026	4, 4, 0.026
4	4, 4, 0.019	8, 6, 0.011	8, 6, 0.011	12, 7, 0.011	16, 8, 0.011	16, 9, 0.011
6	4, 4, 0.026	8, 6, 0.006	9, 6, 0.006	19, 10, 0.005	20, 11, 0.006	64, 25, 0.005
8	4, 4, 0.028	8, 7, 0.002	9, 7, 0.002	22, 13, 0.001	25, 14, 0.001	256, 76, 0.001
10	4, 4, 0.029	8, 7, 0.001	11, 9, 0.0004	21, 14, 0.0004	26, 17, 0.0001	1024, 248, 0.0001
12	4, 4, 0.030	8, 7, 0.001	11, 9, 0.0007	20, 15, 0.0001	27, 19, 0.00001	4096, 840, 0

TABLE I. Maximum and Average bond dimension at end point of simulation (rounded to the nearest integer) for different values of  $\chi$  (on different columns) and the average RMS errors associated with all RDM elements for each simulation. The bond dimensions for the uncompressed MPS (at  $\chi = 0$ ) are also shown for comparison.

$\chi = 10^{-5}$ , though the dynamics is not converged, the key features are preserved. Although the maximum bond dimension, with  $\chi = 10^{-5}$ , is never greater than eight, the resulting error in dynamics is smaller than that produced from a memory truncation of  $L = 20$ . Given how the bond truncation works when applying a MPO to a MPS, even with relatively large values of  $\chi$ , unitarity of propagation is preserved and consequently, the trace is conserved.

## 2. Realistic applications of spin-boson model

The compressed representation enabled by AP-TNPI allows us to span longer memory lengths. This makes it possible to use AP-TNPI to, at least qualitatively, understand the physics of realistic systems. As the first example, consider the charge transfer in the ferrocene-ferrocenium complex in hexane as a solvent. This system was studied using QCPI by one of us [78]. It was shown that the harmonic bath results match the fully atomistic results really well. We apply AP-TNPI to understand the dynamics qualitatively using only short calculations that can be run on extremely modest computational resources.

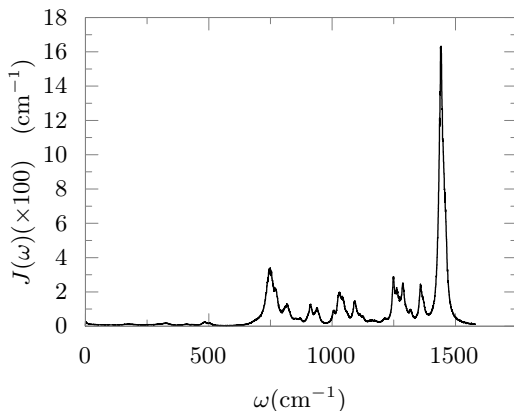


FIG. 7. Spectral density for hexane interacting with ferrocene-ferrocenium.

The system is described by a symmetric TLS Hamiltonian, where  $\hbar\Omega = 32 \text{ cm}^{-1}$  and  $\epsilon = 0$ . As in Eq. (2),

the system is coupled bi-linearly to the bath, which is initially equilibrated with the donor state. The spectral density of the harmonic bath with a reorganization energy of 36 meV [78] is shown in Fig. 7. It is extremely challenging to converge the full dynamics using the basic AP-TNPI framework outlined here because of long memory times, however, we can quite easily converge the initial decay of the population. It is the presence of classical trajectories in QCPI that allows for accelerated convergence with respect to memory length and incorporation of anharmonic effects. Such improvements can, in principle, be added into AP-TNPI, and will be the subject of future research. Here we use the basic AP-TNPI framework outlined in this paper.

For reactions with long time-scales, rate theory can often be used to gain valuable insights. Quantum mechanical rates are typically related to equilibrium correlation functions involving the flux operator,  $\hat{F} = \frac{i}{\hbar} [\hat{H}_0, \hat{h}]$  where  $\hat{h} = |1\rangle\langle 1|$  is the projector on the donor state,  $|1\rangle$  [79–83]. Since the equilibrium of a system coupled to a solvent can often be challenging to compute, it has also been shown that the same information can be obtained from the non-equilibrium flux function [84], which also happens to be related to the instantaneous time-derivative of the donor population. In Fig. 8, we show the short-time dynamics of both the donor population,  $\tilde{\rho}_{11}(t)$ , and the donor flux,  $F(t) = \frac{d\tilde{\rho}_{11}}{dt} = \text{Tr}(\tilde{\rho}(t)\hat{F})$ , as calculated by AP-TNPI. The simulation was run at  $T = 300 \text{ K}$ . Convergence was reached with a time-step of  $\Delta t \approx 12 \text{ fs}$ . These full memory simulations were done for 24 time steps and the truncation cutoff was converged at  $\chi = 10^{-16}$ . In this case, we plot the dynamics corresponding to a maximum bond dimension of  $M = 1000$ , though  $M = 750$  yielded converged results in the timescale shown. A laptop with a total RAM of 8 GB was used for the computation. With access to larger computer memory, it might well be possible to converge the full dynamics directly with AP-TNPI. This real world example is very similar to the sort of parameters that we considered in Fig. 5. The dynamics is a monotonic decay, but still paths containing multiple blips states, i.e. states with  $\Delta s \neq 0$ , are very important. This proves to be exceedingly challenging for BSPI as well.

The population has not decayed to equilibrium within the first 300 fs. However, a lot of information about the

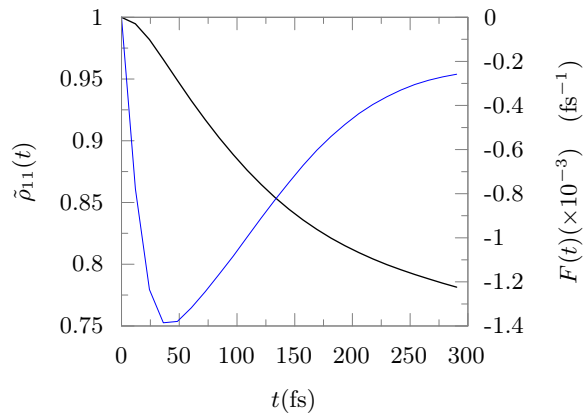


FIG. 8. Population of donor state (black line, left axis) and flux of the donor state (blue line, right axis) as a function of time.

dynamics can be gleaned from a combination of the direct dynamics and the flux function (blue curve). If rate theory is valid, and a slow exponential decay governs the dynamics, then the flux function should quickly plateau at the rate after transients. We see that the flux function in this case shows dramatic changes implying that the transients are not completely over. Combined with the not insignificant population decay, the dramatic changes in the flux function demonstrates the non-exponential nature of the dynamics for this system reproducing the conclusions of the initial exploration [78]. While exact details about the dynamics cannot be inferred unless either the dynamics is simulated to equilibrium or the flux function is simulated to a plateau, it is possible to make intelligent conclusions about the various timescales. The deep drop in the flux function, representing a fast population decay, is followed by a rapid increase, representing a significant slowdown of the transfer dynamics. This large maximum flux out of the donor state, coupled with the non-insignificant decay of population dynamics within the time of simulation allows us to draw intelligent conclusions about the timescales. A “dominant”  $\frac{1}{e}$ -time of  $\sim 720$  fs can be estimated from the maximum flux out of the donor state. Interestingly, this value agrees with the reported  $\frac{1}{e}$ -time of 830 fs calculated from the full QCPI dynamics. The flux curve also shows a significant slowing down of the dynamics in a non-exponential manner. Consequently, traditional equilibrium rate theory would give incorrect rates and predict much longer time-scales. For extremely non-exponential processes like this particular one, it becomes impossible to predict the long-time timescales from such short time dynamics because the flux function does not plateau.

Though the method can be readily extended to larger systems, let us, now, turn our attention to exciton transfer in a dimer. This can be considered the simplest illustrative example of an exciton transfer. Restricting ourselves to the single-exciton Frenkel subspace, we have

a two-level description for the system where  $|\sigma_1\rangle$  corresponds to the first monomer being in the excited state and the second in the ground state; and  $|\sigma_2\rangle$  corresponds to the second monomer being in the excited state and the first in the ground state. The vibrational degrees of freedom of each of the monomers produce a dissipative bath. The Hamiltonian of the bath and its interaction with the system is now given by

$$\hat{H}_b = \sum_{j,b} \frac{p_{jb}^2}{2m_{jb}} + \frac{1}{2} m_{jb} \omega_{jb}^2 \left( x_{jb} - \frac{c_{jb} \hat{V}_j}{m_{jb} \omega_{jb}^2} \right)^2 \quad (38)$$

where the  $b^{\text{th}}$  vibrational mode associated with the  $j^{\text{th}}$  monomer has a frequency of  $\omega_{jb}$  and coupling constant of  $c_{jb}$ . Additionally,  $\hat{V}_j = |\sigma_j\rangle\langle\sigma_j|$  is the projector on to state where the  $j^{\text{th}}$  monomer is excited. This coupling to the system captures the shift of the Born-Oppenheimer surfaces of the localized vibrations between the ground and the excited electronic states of the monomer.

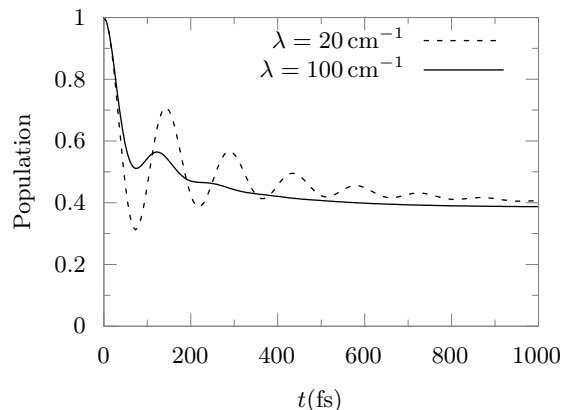


FIG. 9. Excitonic dynamics in a dimer ( $\epsilon = 50 \text{ cm}^{-1}$ ,  $\hbar\Omega = -100 \text{ cm}^{-1}$ ) with a Drude bath with  $\gamma = 53.08 \text{ cm}^{-1}$  at  $T = 300 \text{ K}$ .

Since the two monomers are identical molecules, the spectral densities for the localized molecular vibrations are taken to be identical for both the baths. While AP-TNPI is able to handle discrete rigid vibrations directly, first, we follow Ishizaki and Fleming [85] and assume that the bath is described by a Drude spectral density,

$$J(\omega) = 2\lambda\gamma \frac{\omega}{\omega^2 + \gamma^2}, \quad (39)$$

where  $\lambda$  is the reorganization energy and  $\gamma$  is the cutoff frequency. Figure 9 shows the dynamics of the population corresponding to  $|\sigma_1\rangle$  in the excitonic dimer defined by  $\hbar\Omega = -100 \text{ cm}^{-1}$ ,  $\epsilon = 50 \text{ cm}^{-1}$  and  $\gamma = 53.08 \text{ cm}^{-1}$  at two different values of reorganization energies  $20 \text{ cm}^{-1}$  and  $100 \text{ cm}^{-1}$ . These simulations were performed at room temperature, i.e.,  $T = 300 \text{ K}$ . A time step of  $\Delta t = 6.05 \text{ fs}$  was used with a memory length of  $L = 80$  and a truncation threshold of  $\chi = 10^{-10}$ . The results are

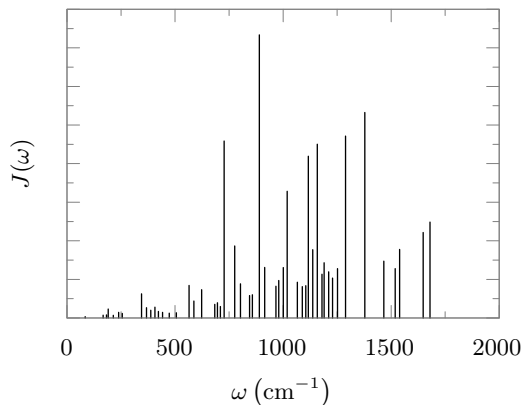


FIG. 10. Vibrational spectral density for a bacteriochlorophyll molecule in arbitrary units with a reorganization energy of  $\lambda = 217.66 \text{ cm}^{-1}$ .

same as the ones reported by Ishizaki and Fleming using HEOM.

Though, till now, we discussed the dynamics corresponding to the Drude spectral density, chlorophyll, being a rigid monomer, has a much more structured, discrete vibrational spectral density. The detailed impact of such structured vibrations on the dynamics cannot be captured by using model spectral densities. Figure 10 shows the spectral density obtained from the Huang-Rhys factors reported by Rätsep *et al.* [86] with a reorganization energy  $\lambda = 217.66 \text{ cm}^{-1}$ . This vibrational bath has already been used to study the quantum dynamics of a bacteriochlorophyll dimer using QCPI [87] and for longer chains and rings [88] using modular path integral [89–91].

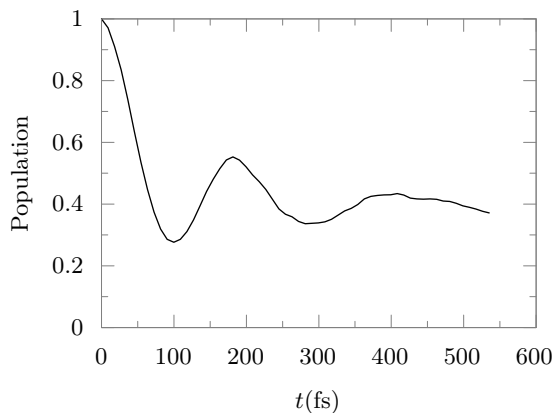


FIG. 11. Excitonic dynamics of the excited monomer in a dimer with the rigid, structured bath given in Fig. 10. The system Hamiltonian is the same as used in Fig. 9.

The dynamics of the same excitonic dimer system under this structured vibrational bath is shown in Fig. 11 using a time step of  $\Delta t = 9.07 \text{ fs}$ . A truncation cutoff of  $\chi = 10^{-9}$  was used. For this simulation, we did

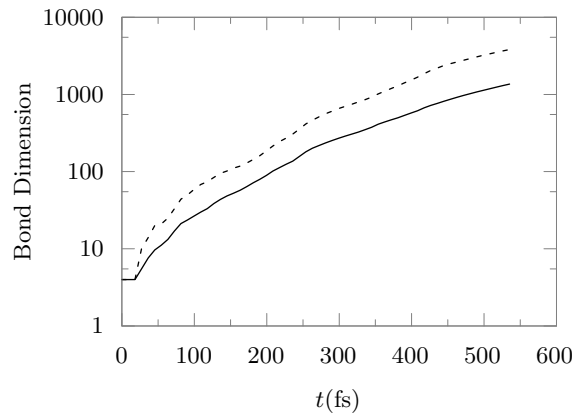


FIG. 12. Growth of average (solid) and maximum (dashed) bond dimensions for the dynamics shown in Fig. 11.

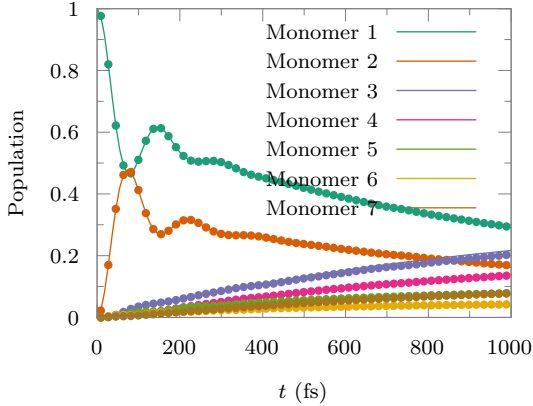
not truncate memory. We note that there are significant differences between Fig. 11 and Fig. 9. It has been shown that increasing the bath reorganization energy,  $\lambda$ , or the characteristic cutoff frequency,  $\gamma$ , leads to a suppression of the electronic oscillations in this system [85]. The first interesting feature is that despite having a large reorganization energy of  $\lambda = 217.66 \text{ cm}^{-1}$  and comprising almost solely of high frequency modes, the dynamics of the system coupled to the discrete bath demonstrate clearer oscillations than those shown when coupled to the Drude bath of less than half the reorganization energy ( $\lambda = 100 \text{ cm}^{-1}$ ). Additionally, the first peak is at  $\sim 175 \text{ fs}$  for the discrete bath, whereas it happens at  $\sim 125 \text{ fs}$  for the  $\lambda = 100 \text{ cm}^{-1}$  Drude bath. Second, there are uneven and irregular properties to the dynamics after  $\sim 300 \text{ fs}$ . Similar, yet more prominent, irregular features have already been reported [87, 88]. These features are due to the absence of a continuous manifold of vibrational states guaranteed by a model spectral density. Since, for simplicity, we are dealing with two isolated bacteriochlorophyll molecules, the vibrational modes are discrete. This is, of course, not the whole story. The presence of a protein scaffolding would lead to a bath common to all the monomers with many ro-translational modes. In principle, we should be able to include such common baths with AP-TNPI as well. In Fig. 12, we plot the average bond dimension as a function of time. Even though these are full memory calculations, the cost clearly does not scale exponentially. It is important to note that the exact characteristics of the time-evolution of the bond-dimension, even within memory, is extremely parameter-dependent.

## B. Multilevel systems

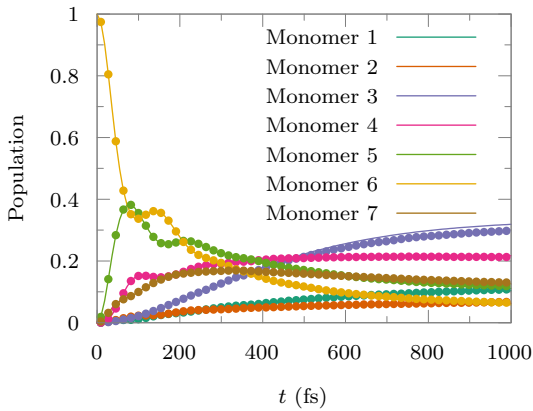
For our first multilevel system example, we extend the exciton model to a system larger than a dimer. The Fenna-Matthew-Olson (FMO) complex is one of the most widely studied light harvesting pigment-protein com-

plexes. A lot of theoretical [92–95] and experimental [86] effort has been expended in order to accurately determine the site energies, electronic couplings and vibrational spectral density of the complex. Additionally, various theoretical methods have been used to study the correspond exciton transfer dynamics. [96–99]. Here, as a simple demonstration, we use the well-known FMO model characterized by the 7-site system Hamiltonian [95]. This model was studied using HEOM by Ishizaki and Fleming [98] using site-local Drude baths describing the local vibrations.[98]

The Hamiltonian describing the bath and its interaction with the system is given by Eq. (38). It has the same structure as that of the excitonic dimer, except with seven sites, corresponding to the unique states in the single excitation subspace. As with the other multi-bath models, all baths are taken to be described by the same spectral density. A site-local Drude spectral density is used with  $\gamma = 106.18 \text{ cm}^{-1}$  and  $\lambda = 35 \text{ cm}^{-1}$ . [98]



(a) Dynamics of the exciton subsequent to excitation of the first monomer.



(b) Dynamics of the exciton subsequent to excitation of the sixth monomer.

FIG. 13. Dynamics of 7-site FMO model. Markers: MTNPI results ( $L = 37$ ). Lines: AP-TNPI results ( $L = 27$ ).

In Fig. 13, we demonstrate the dynamics of the exciton,

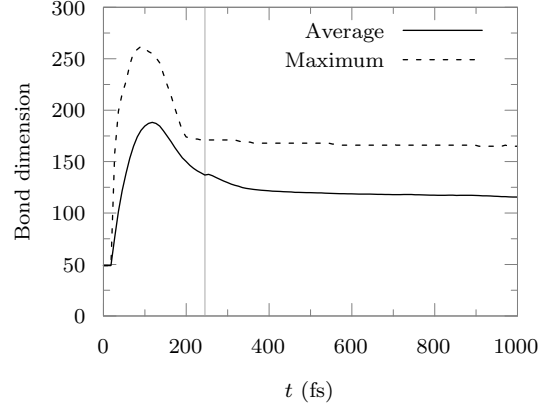


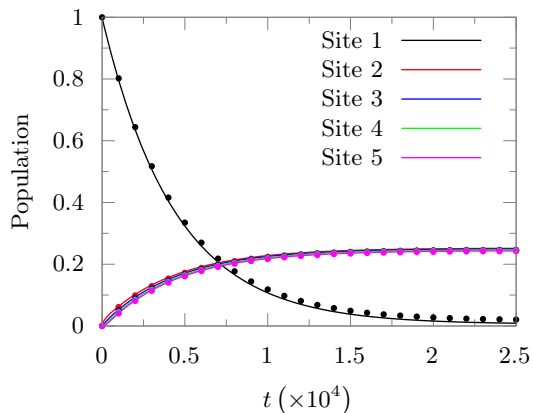
FIG. 14. Growth of average (solid) and maximum (dashed) bond dimension with time for FMO. Gray vertical line indicates the memory span.

at  $T = 300 \text{ K}$ , when the first and the sixth monomers are excited, respectively, reproducing the results previously observed [98]. The IF MPO is obtained as a product of individual IF MPOs corresponding to the local baths of each bacteriochlorophyll monomer as described in Appendix A. The dynamics was converged with a timestep of  $\Delta t = 9.07 \text{ fs}$  and a memory length of  $L = 27$ . The cutoff was converged at  $\chi = 10^{-8}$ . For the MTNPI simulation,  $L = 37$ . We find quite good agreement between the MTNPI and full AP-TNPI results. In Fig. 14, we show the average and maximum bond dimension as a function of time. It is interesting to note that in this case, the bond dimensions starts decreasing even before the memory length is spanned. This is in sharp contrast to most of the other cases, where the bond dimension increases upto memory length and remains approximately constant thereafter. Between Fig. 14 and Fig. 12, it is evident that it is not simple to articulate a unifying rule to predict the evolution of bond dimensions within or beyond memory. It needs to be investigated on a case-by-case basis.

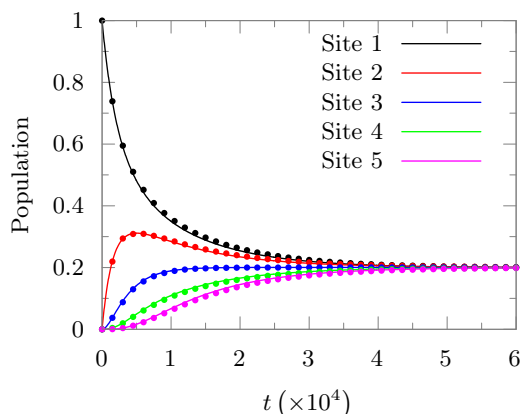
Finally, we explore the dynamics of a multilevel systems with a global solvent. As an application, let us consider a molecular wire for charge transport. The system is described by a tight-binding Hamiltonian with  $N$  sites:

$$\hat{H}_0 = \sum_{1 \leq j \leq D} \epsilon_j |\sigma_j\rangle\langle\sigma_j| - \hbar V \sum_{1 \leq j < D} (|\sigma_j\rangle\langle\sigma_{j+1}| + |\sigma_{j+1}\rangle\langle\sigma_j|) \quad (40)$$

The sites are separated by unit distance. Therefore, the site locations are given by  $\hat{s}|\sigma_j\rangle = (j - 1)|\sigma_j\rangle$  for all  $1 \leq j \leq D$ . The process is started with the  $j = 1$  site being populated. The bath is initially equilibrated with this  $j = 1$  site. The presence of such a global bath prevents use of more recent methods like modular path integrals [89, 90] that are based on the separability of local environments. Following Lambert and Makri [100], we choose  $V = 0.025$  and  $\epsilon_1 = 1$ . For all other sites,



(a) Cold bath,  $\beta = 2$ . Converged memory length  $L = 24$ . MTNPI iteration with  $L = 320$ .



(b) Hot bath,  $\beta = 0.01$ . Converged memory length  $L = 10$ . MTNPI iteration with  $L = 30$ .

FIG. 15. Population dynamics of a molecular wire of chain of length  $D = 5$  described by Eq. (40). Lines represent the MTNPI iteration scheme. Points represent the rigorously correct algorithm.

$1 < j \leq D$ ,  $\epsilon_j = 0$ . The bath is characterized by the Ohmic spectral density defined in Eq. (37) with  $\omega_c = 4$ ,  $\xi = 0.12$ .

In Fig. 15, we show the dynamics of the population for a molecular wire of length,  $D = 5$  at two different inverse temperatures,  $\beta = 2$  (Fig. 15 (a)) and  $\beta = 0.01$  (Fig. 15 (b)). A cutoff of  $\chi = 10^{-7}$  was used for the low temperature calculation, and for the high temperature simulation  $\chi = 10^{-12}$  was used. For both cases, a time-step of  $\Delta t = 0.2$  was used. Because of the structure of this problem, even with such a small cutoff, the maximum bond dimension for both the temperatures was stable at 25, which is also the size of the forward-backward Hilbert space. The average bond dimension decreases to 13.96 for the low temperature case and 15.18 for the high temperature case. The bond dimensions in this problem are significantly smaller than those encountered in some of the two-level system problems, as well as the FMO example. There are two factors responsible for this. First, the

global solvent causes a significant decrease in the probability amplitude for transfer between sites as the distance between them increases. For example, a direct transfer between the first site and the fifth site is extremely improbable because of the high reorganization energies involved. The TNPI filtration scheme seems to take advantage of this and can drastically reduce the bond dimensions of the PA MPSs. Second, because of the definition of the system states,  $\hat{s}|\sigma_j\rangle = (j-1)|\sigma_j\rangle$ , and the coupling to the bath, there are only 9 unique values of  $\Delta s$  as compared to the 25 possible values of the forward-backward state. This leads to a greatly compressed representation of the analytic IF MPO.

The higher temperature bath tends to lead to a sequential transfer of the excess charge, whereas the colder bath leads to an almost simultaneous transfer of population onto all the acceptor sites. The MTNPI scheme is quite accurate: we get the basic features of the dynamics for the low temperature case, and quantitative agreement with the correct dynamics for the high temperature simulation. Though it requires much higher memory lengths to converge, the net time required for the full simulation is orders of magnitude less than the canonical algorithm for iteration. This is because, in the MTNPI scheme, the full complexity of the longer memory only affects the within-memory portion of the simulation. Thereafter, MTNPI abandons the PA tensor and just performs tensor contractions over indices of dimension  $D^2$ , as shown in Eqs. (33) and (34). In contrast, for the canonical and rigorously correct scheme of iteration, the computational complexity remains approximately constant once in the iterative regime of the dynamics. This becomes a significant bottleneck when the iterative regime consists of hundreds of thousands of time steps.

The effective asymmetry in the low temperature case possibly leads the spurious MTNPI memory to increase very rapidly. For the high temperature simulation, the asymmetry is not important on the scale of the thermal energy, and consequently, the spurious MTNPI memory is not as long compared to the converged memory of the full AP-TNPI calculation. Because MTNPI propagates the reduced density matrix of the system from time  $t$  to  $t + L\Delta t$  with an effective augmented propagator, it assumes that the bath and the system are uncorrelated at time  $t$ . We hypothesize that this implicit assumption performs poorly when the asymmetry of the system is important. This would be consistent with what was observed in QCPI [30]. Though this limitation can probably be dealt with in a computationally efficient manner by augmenting MTNPI with the ability to update the augmented propagator to be used in a dynamically consistent manner, it is not important for the purposes of this example.

#### IV. CONCLUSION

System-solvent decomposition is a ubiquitous approach to quantum dynamics in condensed phase where the quantum effects are primarily limited to a low-dimensional subspace. We have presented a tensor network approach to simulating such systems using the quasi-adiabatic propagators and Feynman-Vernon influence functionals. This brings a novel perspective and decomposition to a well-established problem.

Tensor networks utilize certain symmetries in the tensors to obtain highly efficient “factorized” representations. The observation that the entanglement between time-points cannot span temporal lengths greater than that of the non-Markovian memory associated with the bath response function suggests extremely compact matrix-product state representation of the augmented propagator. Because the influence functional can be written as a product of commuting terms, many representations are possible. Here, we have derived an analytic form for the IF MPO that automatically provides a highly efficient and compressed representation without having to resort to numerical optimization techniques. There are well-established techniques for SVD-based and variational optimizations of MPSs that lead to further automatic compression of the PA MPS. This enables us to simulate problems with long non-Markovian memory lengths and with large system sizes, without sacrificing the rigorous nature that characterizes QuAPI-based methods. The structure of AP-TNPI suggests an extremely simple and powerful approximate scheme for computing the reduced density matrix beyond the memory length. This MTNPI method reduces the computational complexity of each step to the cost of a single tensor contraction involving indices with dimension  $D^2$ . Despite introducing additional memory, using it is especially useful when the total time of propagation far exceeds the memory time. Because AP-TNPI already allows us to access long memory lengths, it is not very difficult to span the increased MTNPI memory as well.

After testing the new AP-TNPI framework against benchmark spin-boson simulations, we applied it to study two realistic applications. First, we used a combination of direct dynamics and rate theory to understand the physics of charge transfer in ferrocene-ferrocenium solvated in hexane. These calculations were performed on extremely modest computers and the time-scales that we obtained were consistent with those found in previous QCPI simulations. As a second example of a two-level system, we used AP-TNPI to simulate the exciton dynamics of a chlorophyll dimer with both a Drude bath and a bath of discrete vibrations. We reproduced results obtained by Ishizaki and Fleming [85]. The bath of discrete vibrations leaves some unusual features on the dynamics as compared to the standard model spectral densities. Apart from two-level systems, we also applied AP-TNPI to simulate the dynamics of an exciton in the 7-site model of FMO coupled to local vibrational dissi-

pative environments and a charge transfer in a molecular wire coupled to global solvents. In the molecular wire examples, the computational efficiency of MTNPI could truly be leveraged because the memory length required to be spanned was much shorter than the total time of propagation. Though quite accurate otherwise, it seems to perform comparatively less efficiently when the asymmetry in the system is important. We have postulated a possible solution, that we would explore in the future to make general applications with MTNPI even more accurate. Both the many-site examples show very interesting performance characteristics that have been discussed. Further research is required to properly characterize and understand these differences.

We have demonstrated the wide-ranging applicability of AP-TNPI to a variety of problems using only modest computational resources. From our explorations, it seems that AP-TNPI performs uniformly better than traditional QuAPI. We have also demonstrated the applicability of this method to cases that are extremely challenging even for BSPI. The very recently developed SMatPI and AP-TNPI are substantially different methods and may have complementary benefits. A more thorough investigation would be required to comment on the comparative merits of the two. Future applications would focus on simulation of spectra in various systems such as photosynthetic complexes and an analysis of the effect of a structured spectral density of the bath on these spectra. While the current examples of the excitonic dimer incorporate a local bath, it is possible to incorporate effects of a global ro-translational solvent. This, along with atomistic simulations with classical trajectories, would allow us to evaluate the accuracy of linear response in modeling the protein backbones.

Since AP-TNPI is still a path integral technique, many developments in path integrals involving improved reference propagators [29] and harmonic back reaction [101] to cheaply include anharmonic effects via classical trajectories can be transparently implemented in AP-TNPI. It is well-known that the use of classical trajectory-based reference propagators also lead to an increase of the converged time-steps and decrease the effective memory length [29, 30]. Additionally, a different and extremely promising avenue of exploration relates to application of AP-TNPI to extended systems. Simulations of energy and charge transfer along long molecular chains and aggregates are of particular interest. We have already demonstrated applications of the AP-TNPI framework introduced here to small multi-state systems interacting with a global solvent. However, for longer, extended systems with short-range interaction between sites, the structure of AP-TNPI can also be augmented to decompose the system as a further optimization.

Future development would follow two broad avenues: incorporation of anharmonic and atomistic environments using classical trajectories, and development of spatial decomposition using tensor networks to efficiently work with extended systems containing relatively short-ranged

interactions. We believe that AP-TNPI is a potentially viable framework for developing methods to study the dynamics of several important condensed phase problems.

### ACKNOWLEDGMENTS

We thank Nancy Makri for introducing us to the world of quantum dynamics in general and real time path integrals in particular. A. B. acknowledges the support of the Computational Chemical Center: Chemistry in Solution and at Interfaces funded by the US Department of Energy under Award No. DE-SC0019394. P. W. acknowledges the Miller Institute for Basic Research in Science for funding.

#### Appendix A: Influence Functional for Localized Baths

In Sec. II, we discussed the method primarily for a harmonic bath bilinearly coupled to the “position” operator,  $\hat{s}$ , of the system. However, the influence functionals can be used in a straightforward manner with multiple baths that couple to different system operators. Here we summarize the basic equations [74, 75] and changes to the algorithm required to make AP-TNPI work with the more general bath.

Suppose after QuAPI splitting, the Hamiltonian for independent baths acting through separate system operators is given as

$$\hat{H}_b = \sum_{j,b} \frac{p_{jb}^2}{2m_{jb}} + \frac{1}{2} m_{jb} \omega_{jb}^2 \left( x_{jb} - \frac{c_{jb} \hat{V}_j}{m_{jb} \omega_{jb}^2} \right)^2. \quad (\text{A1})$$

Here for each of the system operators indexed by  $j$ , there is an independent bath with modes indexed by  $b$ . The frequency and coupling of the  $b^{\text{th}}$  mode of the  $j^{\text{th}}$  bath is  $\omega_{jb}$  and  $c_{jb}$  respectively. The  $j^{\text{th}}$  bath interacts with the system through  $\hat{V}_j$ . For path integral calculations, we want to work in a representation of the system where  $\hat{V}_j$  is diagonal for all  $j$ .

The independent baths are specified by the spectral densities

$$J_j(\omega) = \frac{\pi}{2} \sum_b \frac{c_{jb}^2}{m_{jb} \omega_{jb}} \delta(\omega - \omega_{jb}). \quad (\text{A2})$$

which lead to separate  $\eta$ -coefficients for each of the baths. The  $\eta$ -coefficient for the  $j^{\text{th}}$  bath is denoted by  $\eta^j$ . These independent, local baths feature most prominently in descriptions of the local vibrations of monomers in exciton transfer complexes and chromophores.

The only change to the dynamics happens through a change in the influence functional, which becomes a product of all the influence functionals corresponding to the different baths as discussed in Ref. [75]. More specifically, Eq. (8) would now be replaced by

$$F[\{s_n^\pm\}] = \prod_j \exp \left( -\frac{1}{\hbar} \sum_{0 \leq k \leq N} \Delta V_{jk} \sum_{0 \leq k' \leq k} \left( \text{Re}(\eta_{kk'}^j) \Delta V_{jk'} + 2i \text{Im}(\eta_{kk'}^j) \bar{V}_{jk'} \right) \right) \quad (\text{A3})$$

where  $\Delta V_{jk} = V_j(s_k^+) - V_j(s_k^-)$  and  $\bar{V}_{jk} = \frac{V_j(s_k^+) + V_j(s_k^-)}{2}$ . Here, we have summarized Eq. (A5) in the appendix of Ref. [74], or equivalently, Eq. (7) of Ref. [75] using the average and difference coordinates and highlighting the product nature of the total influence functional. Note that the main notational difference from Eq. (7) of Ref. [75] is that we use the  $\hat{V}$  operator to encode the system-solvent coupling for the multibath case instead of simply  $\hat{s}$ . In fact, Nalbach *et al.* [75] go further and discuss the influence functionals for correlated baths on different sites, which have not been used here.

Therefore, instead of having one IF MPO, now there would be as many IF MPOs as there are independent baths. The total IF MPO is defined to be the product of all the individual ones. It is possible to compress these IF MPOs analytically into one single compressed MPO, thereby reducing numerical error, and computational complexity. However, for simplicity this form is not described here.

- 
- [1] L. Zhang, M. Chen, X. Wu, H. Wang, W. E, and R. Car, Deep neural network for the dielectric response of insulators, *Phys. Rev. B* **102**, 1 (2020).
  - [2] M. H. Beck, A. Jäckle, G. A. Worth, and H.-D. Meyer, The multiconfiguration time-dependent Hartree (MCTDH) method: A highly efficient algorithm for propagating wavepackets, *Phys. Rep.* **324**, 1 (2000).
  - [3] H. Wang and M. Thoss, Multilayer formulation of the multiconfiguration time-dependent Hartree theory, *J. Chem. Phys.* **119**, 1289 (2003).
  - [4] S. R. White and A. E. Feiguin, Real-Time Evolution Using the Density Matrix Renormalization Group, *Phys. Rev. Lett.* **93**, 076401 (2004).
  - [5] U. Schollwöck, The density-matrix renormalization group, *Rev. Mod. Phys.* **77**, 259 (2005).
  - [6] H. Ma, Z. Luo, and Y. Yao, The time-dependent density

- matrix renormalisation group method, *Mol. Phys.* **116**, 854 (2018).
- [7] F. D. Maiolo, G. A. Worth, and I. Burghardt, Multi-layer gaussian-based multi-configuration time-dependent hartree (ml-gmctdh) simulations of ultrafast charge separation in a donor-acceptor complex, *The Journal of Chemical Physics* **154**, 144106 (2021).
- [8] D. Picconi and I. Burghardt, Open system dynamics using gaussian-based multiconfigurational time-dependent hartree wavefunctions: Application to environment-modulated tunneling, *The Journal of Chemical Physics* **150**, 224106 (2019).
- [9] T. Jiang, W. Li, J. Ren, and Z. Shuai, Finite temperature dynamical density matrix renormalization group for spectroscopy in frequency domain, *The Journal of Physical Chemistry Letters* **11**, 3761 (2020).
- [10] J. Ren, Z. Shuai, and G. Kin-Lic Chan, Time-dependent density matrix renormalization group algorithms for nearly exact absorption and fluorescence spectra of molecular aggregates at both zero and finite temperature, *Journal of Chemical Theory and Computation* **14**, 5027 (2018).
- [11] Y. Tanimura, Numerically “exact” approach to open quantum dynamics: The hierarchical equations of motion (heom), *J. Chem. Phys.* **153**, 020901 (2020), <https://doi.org/10.1063/5.0011599>.
- [12] J. Liu and W. H. Miller, Using the thermal Gaussian approximation for the Boltzmann operator in semiclassical initial value time correlation functions, *J. Chem. Phys.* **125**, 224104 (2006).
- [13] J. Liu and W. H. Miller, Real time correlation function in a single phase space integral beyond the linearized semiclassical initial value representation, *J. Chem. Phys.* **126**, 234110 (2007).
- [14] R. Gelabert, X. Giménez, M. Thoss, H. Wang, and W. H. Miller, A Log-Derivative Formulation of the Prefactor for the Semiclassical Herman-Kluk Propagator†, *J. Phys. Chem. A* **104**, 10321 (2000).
- [15] R. Gelabert, X. Giménez, M. Thoss, H. Wang, and W. H. Miller, Semiclassical description of diffraction and its quenching by the forward-backward version of the initial value representation, *J. Chem. Phys.* **114**, 2572 (2001).
- [16] V. Guallar, V. S. Batista, and W. H. Miller, Semiclassical molecular dynamics simulations of excited state double-proton transfer in 7-azaindole dimers, *J. Chem. Phys.* **110**, 9922 (1999).
- [17] J. Cao and G. A. Voth, The formulation of quantum statistical mechanics based on the Feynman path centroid density. I. Equilibrium properties, *J. Chem. Phys.* **100**, 5093 (1994).
- [18] J. Cao and G. A. Voth, The formulation of quantum statistical mechanics based on the Feynman path centroid density. II. Dynamical properties, *J. Chem. Phys.* **100**, 5106 (1994).
- [19] I. R. Craig and D. E. Manolopoulos, Quantum statistics and classical mechanics: Real time correlation functions from ring polymer molecular dynamics, *J. Chem. Phys.* **121**, 3368 (2004).
- [20] S. Habershon, B. J. Braams, and D. E. Manolopoulos, Quantum mechanical correlation functions, maximum entropy analytic continuation, and ring polymer molecular dynamics, *J. Chem. Phys.* **127**, 174108 (2007).
- [21] M. Rossi, M. Ceriotti, and D. E. Manolopoulos, How to remove the spurious resonances from ring polymer molecular dynamics, *J. Chem. Phys.* **140**, 234116 (2014).
- [22] J. C. Tully and R. K. Preston, Trajectory Surface Hopping Approach to Nonadiabatic Molecular Collisions: The Reaction of  $H^+$  with  $D_2$ , *J. Chem. Phys.* **55**, 562 (1971).
- [23] D. S. Sholl and J. C. Tully, A generalized surface hopping method, *J. Chem. Phys.* **109**, 7702 (1998).
- [24] J. C. Tully, Perspective: Nonadiabatic dynamics theory, *J. Chem. Phys.* **137**, 22A301 (2012).
- [25] G. Miao, N. Bellonzi, and J. Subotnik, An extension of the fewest switches surface hopping algorithm to complex Hamiltonians and photophysics in magnetic fields: Berry curvature and “magnetic” forces, *J. Chem. Phys.* **150**, 124101 (2019).
- [26] R. Kapral and G. Ciccotti, Mixed quantum-classical dynamics, *J. Chem. Phys.* **110**, 8919 (1999).
- [27] R. Lambert and N. Makri, Quantum-classical path integral. I. Classical memory and weak quantum nonlocality, *J. Chem. Phys.* **137**, 22A552 (2012).
- [28] R. Lambert and N. Makri, Quantum-classical path integral. II. Numerical methodology, *J. Chem. Phys.* **137**, 22A553 (2012).
- [29] T. Banerjee and N. Makri, Quantum-classical path integral with self-consistent solvent-driven reference propagators, *J. Phys. Chem. B* **117**, 13357 (2013).
- [30] P. L. Walters and N. Makri, Iterative quantum-classical path integral with dynamically consistent state hopping, *J. Chem. Phys.* **144**, 044108 (2016).
- [31] Y. Tanimura and R. Kubo, Time Evolution of a Quantum System in Contact with a Nearly Gaussian-Markoffian Noise Bath, *J. Phys. Soc. Japan* **58**, 101 (1989).
- [32] R. P. Feynman and F. L. Vernon, The theory of a general quantum system interacting with a linear dissipative system, *Ann. Phys. (N. Y.)* **24**, 118 (1963).
- [33] N. Makri, The Linear Response Approximation and Its Lowest Order Corrections: An Influence Functional Approach, *J. Phys. Chem. B* **103**, 2823 (1999).
- [34] Y. Tanimura and P. G. Wolynes, Quantum and classical fokker-planck equations for a gaussian-markovian noise bath, *Phys. Rev. A* **43**, 4131 (1991).
- [35] B. Popescu, H. Rahman, and U. Kleinekathöfer, Chebyshev expansion applied to dissipative quantum systems, *J. Phys. Chem. A* **120**, 3270 (2016), pMID: 26845380, <https://doi.org/10.1021/acs.jpca.5b12237>.
- [36] C. Duan, Q. Wang, Z. Tang, and J. Wu, The study of an extended hierarchy equation of motion in the spin-boson model: The cutoff function of the sub-ohmic spectral density, *J. Chem. Phys.* **147**, 164112 (2017), <https://doi.org/10.1063/1.4997669>.
- [37] T. Ikeda and G. D. Scholes, Generalization of the hierarchical equations of motion theory for efficient calculations with arbitrary correlation functions, *J. Chem. Phys.* **152**, 204101 (2020), <https://doi.org/10.1063/5.0007327>.
- [38] N. Makri and D. E. Makarov, Tensor propagator for iterative quantum time evolution of reduced density matrices. I. Theory, *J. Chem. Phys.* **102**, 4600 (1995).
- [39] N. Makri and D. E. Makarov, Tensor propagator for iterative quantum time evolution of reduced density matrices. II. Numerical methodology, *J. Chem. Phys.* **102**, 4611 (1995).

- [40] N. Makri, Exploiting classical decoherence in dissipative quantum dynamics: Memory, phonon emission, and the blip sum, *Chem. Phys. Lett.* **593**, 93 (2014).
- [41] N. Makri, Blip decomposition of the path integral: Exponential acceleration of real-time calculations on quantum dissipative systems, *J. Chem. Phys.* **141**, 134117 (2014).
- [42] N. Makri, Small matrix disentanglement of the path integral: Overcoming the exponential tensor scaling with memory length, *J. Chem. Phys.* **152**, 041104 (2020).
- [43] N. Makri, Small Matrix Path Integral for System-Bath Dynamics, *J. Chem. Theory Comput.* **16**, 4038 (2020).
- [44] A. Leroise, M. Sonner, and D. A. Abanin, Influence Matrix Approach to Many-Body Floquet Dynamics, *Phys. Rev. X* **11**, 21040 (2021).
- [45] S. R. White, Density matrix formulation for quantum renormalization groups, *Phys. Rev. Lett.* **69**, 2863 (1992).
- [46] U. Schollwöck, The density-matrix renormalization group in the age of matrix product states, *Ann. Phys. (N. Y.)* **326**, 96 (2011).
- [47] U. Schollwöck, The density-matrix renormalization group: A short introduction, *Philos. Trans. R. Soc. A Math. Phys. Eng. Sci.* **369**, 2643 (2011).
- [48] E. M. Stoudenmire, L. O. Wagner, S. R. White, and K. Burke, One-Dimensional Continuum Electronic Structure with the Density-Matrix Renormalization Group and Its Implications for Density-Functional Theory, *Phys. Rev. Lett.* **109**, 056402 (2012).
- [49] E. Stoudenmire and S. R. White, Studying Two-Dimensional Systems with the Density Matrix Renormalization Group, *Annu. Rev. Condens. Matter Phys.* **3**, 111 (2012).
- [50] R. Orús, A practical introduction to tensor networks: Matrix product states and projected entangled pair states, *Ann. Phys. (N. Y.)* **349**, 117 (2014).
- [51] G. Vidal, Entanglement Renormalization, *Phys. Rev. Lett.* **99**, 220405 (2007).
- [52] G. Vidal, Class of quantum Many-Body states that can be efficiently simulated, *Phys. Rev. Lett.* **101**, 1 (2008).
- [53] A. Strathearn, P. Kirton, D. Kilda, J. Keeling, and B. W. Lovett, Efficient non-Markovian quantum dynamics using time-evolving matrix product operators, *Nat. Commun.* **9**, 1 (2018).
- [54] M. R. Jørgensen and F. A. Pollock, Exploiting the Causal Tensor Network Structure of Quantum Processes to Efficiently Simulate Non-Markovian Path Integrals, *Phys. Rev. Lett.* **123**, 240602 (2019).
- [55] E. Ye and G. K.-L. Chan, Constructing tensor network influence functionals for general quantum dynamics, *J. Chem. Phys.* **155**, 044104 (2021).
- [56] A. Bose, A pairwise connected tensor network representation of path integrals (2021), [arXiv:2106.14934](https://arxiv.org/abs/2106.14934) [quant-ph].
- [57] N. Makri, Improved Feynman propagators on a grid and non-adiabatic corrections within the path integral framework, *Chem. Phys. Lett.* **193**, 435 (1992).
- [58] N. Makri, On smooth Feynman propagators for real time path integrals, *J. Phys. Chem.* **97**, 2417 (1993).
- [59] M. Cygorek, M. Cosacchi, A. Vagov, V. M. Axt, B. W. Lovett, J. Keeling, and E. M. Gauger, Numerically-exact simulations of arbitrary open quantum systems using automated compression of environments, [arXiv:2101](https://arxiv.org/abs/2101) (2021).
- [60] ITensor Library (version 3.0.0), ITensor Libr. (version 3.0.0) <https://itensor.org>.
- [61] A. O. Caldeira and A. J. Leggett, Path integral approach to quantum Brownian motion, *Phys. A Stat. Mech. its Appl.* **121**, 587 (1983).
- [62] G. K. L. Chan, A. Keselman, N. Nakatani, Z. Li, and S. R. White, Matrix product operators, matrix product states, and ab initio density matrix renormalization group algorithms, *J. Chem. Phys.* **145**, 10.1063/1.4955108 (2016).
- [63] D. E. Parker, X. Cao, and M. P. Zaletel, Local matrix product operators: Canonical form, compression, and control theory, *Phys. Rev. B* **102**, 35147 (2020).
- [64] E. Sim and N. Makri, Filtered propagator functional for iterative dynamics of quantum dissipative systems, *Comput. Phys. Commun.* **99**, 335 (1997).
- [65] M. Richter and B. P. Fingerhut, Coarse-grained representation of the quasi adiabatic propagator path integral for the treatment of non-Markovian long-time bath memory, *J. Chem. Phys.* **146**, 214101 (2017).
- [66] S. Nakajima, On Quantum Theory of Transport Phenomena, *Prog. Theor. Phys.* **21**, 659 (1958).
- [67] R. Zwanzig, Ensemble method in the theory of irreversibility, *J. Chem. Phys.* **33**, 1338 (1960).
- [68] Q. Shi and E. Geva, A new approach to calculating the memory kernel of the generalized quantum master equation for an arbitrary system–bath coupling, *J. Chem. Phys.* **119**, 12063 (2003).
- [69] A. Montoya-Castillo and D. R. Reichman, Approximate but accurate quantum dynamics from the Mori formalism: I. Nonequilibrium dynamics, *J. Chem. Phys.* **144**, 184104 (2016).
- [70] A. Kelly, A. Montoya-Castillo, L. Wang, and T. E. Markland, Generalized quantum master equations in and out of equilibrium: When can one win?, *J. Chem. Phys.* **144**, 184105 (2016).
- [71] L. Kidon, H. Wang, M. Thoss, and E. Rabani, On the memory kernel and the reduced system propagator, *J. Chem. Phys.* **149**, 104105 (2018).
- [72] S. Chatterjee and N. Makri, Real-Time Path Integral Methods, Quantum Master Equations, and Classical vs Quantum Memory, *J. Phys. Chem. B* **123**, 10470 (2019).
- [73] S. Paeckel, T. Köhler, A. Swoboda, S. R. Manmana, U. Schollwöck, and C. Hubig, Time-evolution methods for matrix-product states, *Ann. Phys. (N. Y.)* **411**, 167998 (2019).
- [74] J. Strümpfer and K. Schulten, Light harvesting complex II B850 excitation dynamics, *J. Chem. Phys.* **131**, 225101 (2009).
- [75] P. Nalbach, J. Eckel, and M. Thorwart, Quantum coherent biomolecular energy transfer with spatially correlated fluctuations, *New J. Phys.* **12**, 0 (2010).
- [76] P. L. Walters, T. Banerjee, and N. Makri, On iterative path integral calculations for a system interacting with a shifted dissipative bath, *J. Chem. Phys.* **143**, 074112 (2015).
- [77] N. Makri, Small matrix path integral with extended memory, *J. Chem. Theory Comput.* **17**, 1.
- [78] P. L. Walters and N. Makri, Quantum–Classical Path Integral Simulation of Ferrocene–Ferrocenium Charge Transfer in Liquid Hexane, *J. Phys. Chem. Lett.* **6**, 4959 (2015).
- [79] W. H. Miller, Semiclassical limit of quantum mechanical transition state theory for nonseparable systems, *J.*

- Chem. Phys. **62**, 1899 (1975).
- [80] W. H. Miller, S. D. Schwartz, and J. W. Tromp, Quantum mechanical rate constants for bimolecular reactions, *J. Chem. Phys.* **79**, 4889 (1983).
- [81] K. Yamashita and W. H. Miller, “Direct” calculation of quantum mechanical rate constants via path integral methods: Application to the reaction path Hamiltonian, with numerical test for the H+H<sub>2</sub> reaction in 3D, *J. Chem. Phys.* **82**, 5475 (1985).
- [82] M. Topaler and N. Makri, Quantum rates for a double well coupled to a dissipative bath: Accurate path integral results and comparison with approximate theories, *J. Chem. Phys.* **101**, 7500 (1994).
- [83] A. Bose and N. Makri, Quantum-classical path integral evaluation of reaction rates with a near-equilibrium flux formulation, *Int. J. Quantum Chem.*, 1 (2021).
- [84] A. Bose and N. Makri, Non-equilibrium reactive flux: A unified framework for slow and fast reaction kinetics, *J. Chem. Phys.* **147**, 152723 (2017).
- [85] A. Ishizaki and G. R. Fleming, Unified treatment of quantum coherent and incoherent hopping dynamics in electronic energy transfer: Reduced hierarchy equation approach, *J. Chem. Phys.* **130**, 234111 (2009).
- [86] M. Rätsep, Z.-L. Cai, J. R. Reimers, and A. Freiberg, Demonstration and interpretation of significant asymmetry in the low-resolution and high-resolution Q<sub>y</sub> fluorescence and absorption spectra of bacteriochlorophyll a, *J. Chem. Phys.* **134**, 024506 (2011).
- [87] A. Bose and N. Makri, All-Mode Quantum-Classical Path Integral Simulation of Bacteriochlorophyll Dimer Exciton-Vibration Dynamics, *J. Phys. Chem. B* **124**, 5028 (2020).
- [88] S. Kundu and N. Makri, Real-Time Path Integral Simulation of Exciton-Vibration Dynamics in Light-Harvesting Bacteriochlorophyll Aggregates, *J. Phys. Chem. Lett.* **11**, 8783 (2020).
- [89] N. Makri, Modular path integral methodology for real-time quantum dynamics, *J. Chem. Phys.* **149**, 214108 (2018).
- [90] N. Makri, Communication: Modular path integral: Quantum dynamics via sequential necklace linking, *J. Chem. Phys.* **148**, 101101 (2018).
- [91] S. Kundu and N. Makri, Modular path integral for discrete systems with non-diagonal couplings, *J. Chem. Phys.* **151**, 074110 (2019).
- [92] C. Olbrich and U. Kleinekathöfer, Time-Dependent Atomistic View on the Electronic Relaxation in Light-Harvesting System II, *J. Phys. Chem. B* **114**, 12427 (2010).
- [93] C. Olbrich, J. Strümpfer, K. Schulten, and U. Kleinekathöfer, Theory and Simulation of the Environmental Effects on FMO Electronic Transitions, *J. Phys. Chem. Lett.* **2**, 1771 (2011).
- [94] T. Renger, A. Klinger, F. Steinecker, M. Schmidt am Busch, J. Numata, and F. Müh, Normal Mode Analysis of the Spectral Density of the Fenna–Matthews–Olson Light-Harvesting Protein: How the Protein Dissipates the Excess Energy of Excitons, *J. Phys. Chem. B* **116**, 14565 (2012).
- [95] J. Adolphs and T. Renger, How Proteins Trigger Excitation Energy Transfer in the FMO Complex of Green Sulfur Bacteria, *Biophys. J.* **91**, 2778 (2006).
- [96] P. Nalbach and M. Thorwart, The role of discrete molecular modes in the coherent exciton dynamics in FMO, *Journal of Physics B: Atomic, Molecular and Optical Physics* **45**, 154009 (2012).
- [97] G. Tao and W. H. Miller, Semiclassical Description of Electronic Excitation Population Transfer in a Model Photosynthetic System, *J. Phys. Chem. Lett.* **1**, 891 (2010).
- [98] A. Ishizaki and G. R. Fleming, Theoretical examination of quantum coherence in a photosynthetic system at physiological temperature, *Proc. Natl. Acad. Sci.* **106**, 17255 (2009).
- [99] E. Mulvihill, K. M. Lenn, X. Gao, A. Schubert, B. D. Dunietz, and E. Geva, Simulating energy transfer dynamics in the Fenna–Matthews–Olson complex via the modified generalized quantum master equation, *J. Chem. Phys.* **154**, 204109 (2021).
- [100] R. Lambert and N. Makri, Memory propagator matrix for long-time dissipative charge transfer dynamics, *Mol. Phys.* **110**, 1967 (2012).
- [101] F. Wang and N. Makri, Quantum-classical path integral with a harmonic treatment of the back-reaction, *J. Chem. Phys.* **150**, 184102 (2019).